Acta Materialia 261 (2023) 119380

Contents lists available at ScienceDirect

Acta Materialia

journal homepage: www.elsevier.com/locate/actamat

Full length article

High-temperature microstructure evolution of an advanced intermetallic nano-lamellar γ-TiAl-based alloy and associated diffusion processes

María L. Nó [a,*], Thomas Klein [b], Helmut Clemens [c], Jose M. San Juan [a]

[a] Departamento de Física, Facultad de Ciencia y Tecnología, Universidad del País Vasco, UPV/EHU, Apdo 644, Bilbao 48080, Spain
[b] LKR Light Metals Technologies, AIT Austrian Institute of Technology, Ranshofen 5282, Austria
[c] Department of Materials Science, Montanuniversität Leoben, Roseggerstr. 12, Leoben 8700, Austria

ARTICLE INFO

Keywords:
Intermetallics
Titanium aluminides
Electron microscopy
Precipitation behavior
Diffusion mechanism

ABSTRACT

Nano-lamellar advanced γ-TiAl based alloys doped with small amounts of C and Si are being developed to improve the creep resistance in order to increase the performances of this kind of alloys applied in the low-pressure turbine of aircraft engines. In order to extend the service temperature up to 1073 K or even above, the control of the microstructure stability is key. In this work, a complete study of the microstructure evolution during high-temperature exposure up to 1153 K has been approached through different electron microscopy techniques including HRTEM and HRSTEM with microanalysis. The nucleation and growth of the ordered β_o precipitates and the ζ silicides inside the α_2 lamellae has been carefully characterized and new orientation relationships and the misfit between all crystalline lattices has been determined, as well as the chemical concentration of the different atomic species on each phase. The electron microscopy study shows that β_o and ζ precipitates inside α_2 prevents or retards the dissolution of the α_2 lamellae and its final disintegration in favor of the γ lamellae. This phenomenon has been discussed in terms of the phase coherence and diffusion processes. These important results allow conclude that the coarsening of the γ lamellae is delayed because of the β_o and ζ precipitation, allowing to explain the observed enhancement of the creep resistance in this γ-TiAl based alloy exhibiting a nano-lamellar microstructure.

1. Introduction

Nowadays, aero-engine manufacturers are facing new challenges to significantly contribute to the "Clean Planet for All" international strategy [1] and one of the main targets is to exceed the present service operation temperature to increase the overall engine efficiency in order to sustainably reduce the so-called greenhouse gas emission. Indeed, according the last report of the European Union Aviation Safety Agency (EASA) [1], at present the full-flight CO_2 emissions have doubled since 1990. To revert this trend, the "2050 low carbon economy" road map of the EU [2] proposes the target of cutting the greenhouse gas emissions by 80 % with respect to the 1990 levels. This scenario was already anticipated by the international scientific community, which since 1990 underwent multiple research programs on intermetallic multi-phase γ-TiAl based alloys, as the main candidate material to fulfill the requirements to improve the engine efficiency, see the overviews [3–11] to follow the progress in this field. As a consequence of such developments, two different families of γ-TiAl alloys, the named 48–2–2 alloy [3] and the TNM alloy [9] are already being used in the low pressure turbine of advanced eco-friendly aero-engines, e.g. see [10,11]. The use of such light-weight γ-TiAl based alloys offers an advantage, the reduction of the greenhouse gas emissions [12], but still significant improvements are required to fulfill the target of the above mentioned "Clean Planet for All" strategy. In order to reach this goal, one of the key factors is to improve the creep resistance at elevated temperatures. The progress in this direction, however, requires a deep knowledge and mastering of the creep controlling microscopic mechanisms.

Among the different aspects that must be considered, the γ/α_2 spacing within the lamellar colonies is a crucial parameter controlling creep resistance [13–15]. Indeed, the plastic deformation of γ/α_2 lamellar colonies proceed by the gliding in γ-lamellae of the $b = 1/2 <110]$ dislocation loops emitted from the semicoherent γ_1/γ_2 or γ/α_2 interfaces [3,6]. However, the line tension model [16,17] employed to describe the behavior of these dislocation loops in TiAl [6,18] predicts that the mechanism of growing and moving of such loops is prevented when the thickness of the lamella decrease and eventually could be fully

* Corresponding author.
E-mail address: maria.no@ehu.es (M.L. Nó).

https://doi.org/10.1016/j.actamat.2023.119380
Received 30 June 2023; Received in revised form 17 September 2023; Accepted 22 September 2023
Available online 4 October 2023

blocked below a critical value, which could be estimated at about 50 nm. Consequently, the development of nano-lamellar TiAl alloys becomes as an efficient method to improve creep resistance at high temperature [19].

Once dislocation gliding is assumed to be blocked, diffusion and dislocation-climb processes can be invoked as responsible for creep [6]. Regarding the atomic diffusion processes in intermetallic TiAl alloys, the diffusion coefficients of the different atomic species, in particular Ti and Al, were measured for both phases γ and α_2 [20–25]. Moreover the activation energies of the relaxation processes associated with the short distance diffusion of the different atomic species in γ, α_2 and β_o phases [26–30], as well as the corresponding diffusion coefficients [31], were measured by internal friction (IF). In addition, recent works show that the combined addition of C and Si to the TNM alloys [32–34] significantly improves the creep behavior of TNM$^+$ alloys [35,19]. Nevertheless, diffusion processes taking place at high temperature slowly modify the microstructure, such as was observed during creep [19]. However, to fulfill the needed creep performance the microstructure of the alloy must be thermally stable or to exhibit a controlled slow evolution, as assumed for creep in commercial superalloys [36]. Consequently, a detailed characterization of the microstructure is required to understand the mechanisms involved in such modification.

The aim of the present work is to perform this microstructural characterization in the nano-lamellar TNM$^+$ alloys, by using several techniques of electron microscopy, including high-resolution TEM (HRTEM) and high-resolution scanning-transmission electron microscopy (HRSTEM), together with a powerful X-ray micro/nano analysis. The study of the nano-lamellar microstructure, before and after the high-temperature thermal exposure during IF measurements, is approached in a comparative way in order to elucidate the microstructure changes. The observed evolution is finally discussed in terms of the diffusion processes occurring at high temperature, which were studied on the same alloy [29,31].

2. Materials and methods

2.1. Materials

The present work is focused on the γ-TiAl based alloy named TNM$^+$, whose chemical composition is Ti-43.3Al-4.02Nb-0.96Mo-0.12B-0.34C-0.31Si (in at.%). This alloy is based on the TNM alloying concept [7], but refined with nominal additions of 0.3 at.% C and 0.3 at.% Si. The material was processed by plasma arc melting and supplied by Hanseatische Waren Handelsgesellschaft mbH & Co KG, Bremen, Germany. After casting, the material was subjected to hot-isostatic pressing (HIP) at 1473 K for 240 min at a maximum pressure of 200 MPa to close residual casting porosity and to homogenize the microstructure. Subsequently, a two-step heat treatment under atmospheric conditions was applied in order to adjust a nano-lamellar microstructure [19]. The first step, the homogenization treatment, was conducted in the single α-phase field region, slightly above the γ-solvus temperature, at 1553 K for 30 min followed by air-cooling (AC). Then an aging treatment was performed at 1173 K for 180 min followed by furnace cooling (FC), in order to develop a microstructure consisting of α_2/γ-colonies exhibiting a lamellar spacing in the range of few nanometers.

The initial (I) microstructure before the IF and creep tests, sample named TNM$^+$*I*, and the final (F) microstructure after IF measurements (twelve runs at 1.5 K/min up to 1153 K, [29]), sample named TNM$^+$*F*, were characterized and compared in order to elucidate the influence of the thermal exposure.

2.2. Electron microscopy

Schottky field emission scanning electron microscopes (SEM), JEOL JSM-7000F and FEI Focus Ion Beam Helios 650, equipped with back-scatter electron (BSE) detectors, Oxford energy dispersive X-ray spectrometer (EDX) and Nordlys II HKL electron back-scattered diffraction (EBSD) detector, were employed to characterize the overall microstructure of the electrolytically polished samples (Struers Lectropol-5 with A3 electrolyte). The SEM were operated at 5 and 10 kV voltages with beam currents between 0.4 and 1 nA. The average colony size was determined on BSE images by means of the linear intercept method.

The characterization of the samples by transmission and scanning-transmission electron microscopy (TEM and STEM) was carried out on a FEI Titan Cubed G2 60–300 kV with a gun monochromator, a Cs-objective aberration corrector (CEOS) and a super-X detector, with four X-ray silicon drift detectors, installed at the Basque Country University. The 3 mm diameter thin foils, obtained by the twin jet electropolishing technique (Struers Tenupol 5 with A3 electrolyte) were observed by TEM/STEM at 200 kV or 300 kV. Bright and dark field (BF, DF) as well as selected area diffraction (SADP) modes were employed. Additionally, the FEI Titan is equipped with three condenser lenses, therefore, able to produce a truly parallel beam from 200 nm in diameter, without using any selection area aperture, allowing micro and nano diffraction in parallel mode. High-angle annular dark field (HAADF), as well as qualitative and quantitative EDX maps, were employed in STEM. For the EDX maps, beam currents between 0.08 and 0.36 nA, 900 s per map with scans of 6 s, and a drift correction system were used. The quantitative analysis was done considering a thickness of 90 nm and the Cliff-Lorimer factors. High-resolution images were acquired in TEM and STEM modes (HRTEM, HRSTEM) and the Fourier transform (FT) of the HRTEM/HRSTEM images were also obtained. Lamellar spacing was determined by means of the linear intercept method on HAADF images in edge-on condition (interface parallel to the e-beam). In the STEM-HAADF images the contrast is related to the atomic number, Z; therefore the α_2 laths appear brigther than the γ laths. DF images were also used to corroborate the α_2 versus γ volume fraction, as well as the kind of γ variants.

3. Experimental results

3.1. General description of the microstructure

The microstrucuture of the sample TNM$^+$*I* was previously described [19,29], and the overall microstructure of sample TNM$^+$*F* is similar, consisting of α_2+γ lamellar colonies with signs of discontinuous precipitation (DP) at the colony boundaries, as shown in the supplementary S1. The mean size of the colonies is also similar in both samples: $\phi_I = 29 \pm 3$ μm and $\phi_F = 30.0 \pm 0.2$ μm. . However in the particular case of the TNM$^+$*F* sample, many precipitates of very small size are observed inside the colonies, in the surrounding area of the triple points and some DP zones (arrows F in supplementary information S1).

Fig. 1a shows the BF image of the precipitates taken on sample TNM$^+$*F* inside a DP region in between the lamellar colonies labeled as I and II. From the quantitative analysis of the EDX maps (see supplementary information, S2-Fig. 1b), the composition of the different precipitates was obtained and is presented in Fig. 1b. The EDX map of C shows that the α_2 phase and the precipitate 1 are richer in C than the other phases; C cannot be correctly quantified from EDX. The identification of the phases, proposed on the base of the quantitative EDX maps, was corroborated through parallel nano diffraction. Fig. 1c shows a nano diffraction pattern of the Si-rich precipitate, named as 1 in Fig. 1a, which is indexed from the different high-symmetry zone axis as Ti_5Si_3 ($P6_3/mcm$) [37] (see supplementary information, S3-Fig. 1c), with the lattice parameters measured in the present sample: $a = b = 0.787$ nm and $c = 0.543$ nm. From the Table in Fig. 1b, it can be deduced that the Si-rich precipitates (21.5 at% Si), which show a higher Nb content than the matrix, correspond to the phase $(Ti, Nb, Mo)_5 (Si, Al)_3$, termed ζ in the literature [38], whereas the precipitates with high Mo content correspond to the ordered β_o phase. Finally, it is worth of remark that in the region close to the DP (colony I), some very small precipitates, thin and

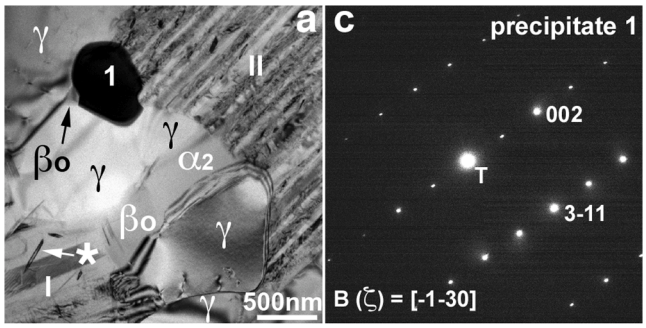

b

Atomic-%	Al	Si	Ti	Nb	Mo
γ	46	1.1	46.3	4.3	2.3
1 - ζ	16.9	21.5	49.4	8.4	3.8
β_o	33.4	1.1	51.1	6.1	8.3
α_2	31.4	1.1	60.7	4.3	2.5

Fig. 1. DP between colonies I and II in TNM$^+$*F* sample, TEM/STEM at 200 kV. (a) TEM-BF image. (b) Quantitative analysis from STEM-EDX maps. (c) Parallel nano diffraction pattern (ϕ_{beam}=570 nm) in the precipitate ζ labeled 1. (*) Small Mo-rich precipitate.

elongated (*l*<300 nm), with a high Mo content (indicated with * in Figs. 1a and S2-Fig 1b) are observed. Such precipitates appear only in the sample TNM$^+$*F* and exhibit several orientation relationships with respect to the α_2 phase of colony I, such as is observed in the HAADF images and the Mo-map shown in the supplementary information, see S4-Fig. 1. Their lattice parameter is $a = 0.3192$ nm (Pm-3m), and the precipitates are indexed as β_o phase [39], as displayed in the convergent nano diffraction pattern of S4-Fig. 1. Hence, this result proves that the precipitates observed around of the triple points and within the DP zone in samples TNM$^+$*F* (arrows F in S1) correspond to β_o phase.

In case of sample TNM$^+$*I*, the TEM-BF image of Fig. 2 shows a small area of a triple point between lamellar colonies. The triple point is rich in Mo and corresponds to the β_o phase labeled A (see supplementary information, S5-Fig. 2). It can be observed that inside this precipitate A, there are several small precipitates (denoted as B) and some of them are anchoring dislocations. The lamellar colonies surrounding the triple point penetrate into the β_o precipitate and its lamellae exhibit a high density of small precipitates at the lamellae tips (C) or at its lateral sides

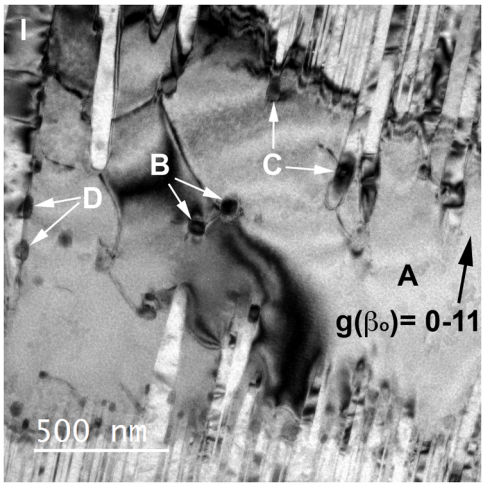

Fig. 2. TEM image, BF at 300 kV, taken in the TNM$^+$*I* sample at a triple junction of three lamellar colonies. Label A indicates β_o phase and label B indicates small precipitates inside the β_o phase. Label C are small precipitates at the end of the α_2 lamellae. Label D indicates precipitates in the lateral side of a γ lamella.

(D). The HAADF image of Fig. 3a as well as the qualitative and quantitative EDX maps show that the B precipitates are quadrangular (lateral lengths ~ 60 nm) and have a higher Si and Nb content and a lower Mo content than the surrounding β_o phase. Fig. 3b shows the parallel beam nano diffraction pattern of the area presented in Fig. 3a, taken in edge-on condition at the interfaces between the precipitates B and the β_o phase. The indexation of the pattern gives evidence that these small particles are ζ precipitates with the following orientation relationship (OR) respect to β_o:

$(110)_{\beta_o} \| (300)_\zeta$ *at the flat interfaces* 1

$(\bar{1}10)_{\beta_o} \| (\bar{1}2\bar{2})_\zeta$ *at the flat interfaces* 2

and

$[001]_{\beta_o} \| [011]_\zeta$ *in both cases*

The OR of the B1 precipitate with β_o was confirmed by HRSTEM-HAADF in Fig. 3c, whose noise was filtered using the Fourier transform of the original images. Fig. 3c shows the flat interfaces (1) and (2) between the B1 precipitate and the β_o phase, and in Fig. 3d the unit lattices of the β_o and ζ phases show the same orientation than in Figs. 3b, c. In Fig. 3c, the atomic columns of Ti and Al(Mo, Nb, Si) are well observed in the ordered β_o phase as well as some of the atomic columns of the Ti(Mo, Nb) of the silicide, although those atomic columns enclosed in a circle in the simulated image of Fig. 3d cannot be resolved because they are at a smaller distance than the spatial resolution, i.e. 0.135 nm in HRSTEM mode. Taking into account the atomic lattices shown in Fig. 3d and the images in Fig. 3c, it can be concluded that a perfect continuity of the atomic planes $(110)_{\beta_o} \| (300)_\zeta$ occurs at interface 2, whereas a small misfit appears along the atomic planes $(\bar{1}10)_{\beta_o} \| (\bar{1}2\bar{2})_\zeta$ at interface 1.

Now to the precipitates formed at the boundaries of the lamellae penetrating inside the β_o phase precipitated in between three colonies, denoted as C in Fig. 2. The STEM-EDX map of Fig. 4a show that such small precipitates have a high Si content and they are placed at the tip of the α_2 lamellae (precipitate 1) or in the lateral face of the broader γ lamellae (precipitate 2) as can be also observed in the S6-Fig. 4a of the supplementary information. These silicides show a Moire's fringes contrast because their sizes are smaller than the thickness of the sample. All precipitates exhibit Moire's fringes with the same orientation and the diffraction patterns confirm the orientation of the atomic planes of both phases:

$(110)_{\beta_o} \| (300)_\zeta$

The HRSTEM-HAADF and HRTEM images taken in the lamella in contact with precipitate 1, Fig. 4b, as well as their FT, confirm that this silicide was formed at the extremity of the α_2 lath. A similar result is obtained for the precipitate 2 at the lateral side of the γ lamella. These atomic resolution images, together with the parallel nano diffraction patterns of the lamellae and precipitates in Fig. 4c, show that there is an OR between the atomic planes of the silicides and the α_2 and γ phases:

$(300)_\zeta \parallel (002)_{\alpha_2} \parallel \{111\}_\gamma$

The six different orientations of the variants of γ lamellae with respect to the α_2 phase are denoted as V1 to V6 [40,41], and the same code will be used in the present work. It should be remarked that in the diffraction condition of Fig. 4c the variant V2 is indistinguishable from V6, and the same applies for variants V3 and V5.

3.2. Lamellar colonies before IF

In TNM$^+$*I* samples the colonies are constituted by α_2 and γ laths with rather flat interfaces, in which interfacial steps and interface dislocations were observed [29]. The α_2 phase volume fraction, measured in

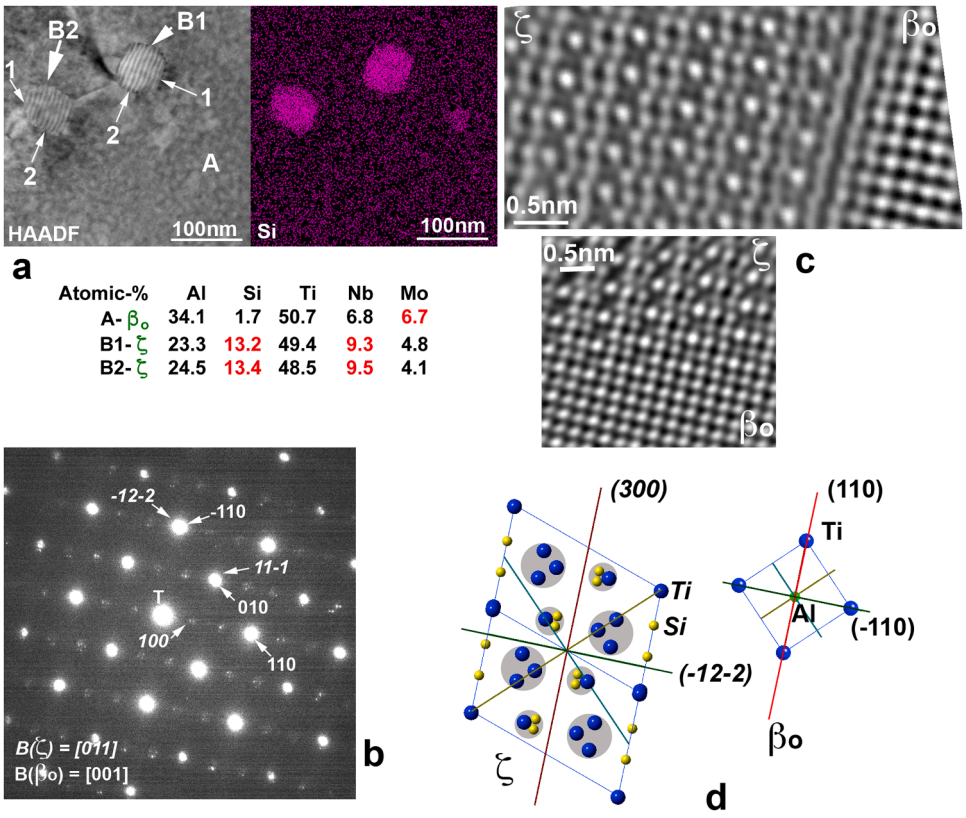

Fig. 3. Characterization of the small precipitates B1 and B2 inside the β_o phase indicated in Fig. 2; TEM/STEM at 300 kV. (a) STEM-HAADF image and the corresponding EDX map of Si (I_{beam}=0.250 nA) and composition of the precipitates obtained from the quantification of the EDX maps; (b) parallel nano diffraction pattern (ϕ_{beam}= 265 nm) taken in edge-on condition for the interfaces 1 and 2 from image (a); (c) HRSTEM-HAADF images including the interfaces 1 and 2 between the ζ silicide B1 and the β_o phase, labeled as A in the image (a). The images were noise-cleaned using the Fourier Transform (FT) of the original image; (d) Single crystal lattices oriented as in Figs. (b) and (c) for the ζ silicide B1 and the β_o phase; the encircled atoms cannot be distinguished in the HAADF images of (c).

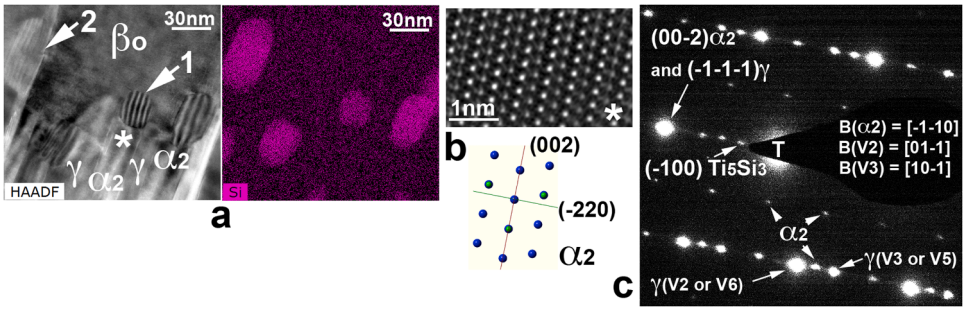

Fig. 4. TNM$^+$*I* sample; TEM/STEM at 300 kV. Small precipitates at the interface between the β_0 phase and the colonies shown in Fig. 2. (a) STEM-HAADF image and the corresponding qualitative EDX map of Si (I_{beam}= 0.250 nA); (b) HRTEM, after noise cleaning by the FT, from the α_2 phase at the (*) location in (a), and its crystal lattice oriented as in the HRTEM image; (c) parallel nano diffraction pattern (ϕ_{beam}= 350 nm) from an area including Fig. (a); labels V2, V3, V5 and V6 identify four of the six possible γ variants, with the common plane (111)γ, which is parallel to the (002)α_2 plane.

STEM-HAADF mode, is 27 % and the HRSTEM-HAADF images showed that the thinnest α_2 lath is 0.46 nm wide, whereas the thickest one measured 33 nm [29]. The γ lamellae have, in average, a thickness less than 60 nm, although some of them reach a width of up to 125 nm. Generally, the internal part of the colonies is free of precipitates except some small ones ($\phi \leq 15$ nm), which exist usually isolated inside the lamellae, see Fig. 5, as well as some other slightly bigger ones ($\phi \leq 70$ nm) at the extremity of some lamellae, e.g. see Fig. 6.

The HAADF image of Fig. 5a shows a small precipitate ($\phi \approx 10$ nm) labeled (1) that has nucleated inside an α_2 lath and has a high Mo content, as shown in the Table of Fig. 5b, obtained from quantitative EDX maps of the different phases. The composition of the precipitate (1) shown in Fig. 5a, together with the FT obtained from the HRSTEM image of a small region of the precipitate (Fig. 5c) allow its identification as β_o phase. Another small Mo-rich precipitate is characterized in the supplementary information (see S7-Fig. 5). These results seem to indicate that β_o precipitates nucleate inside the α_2.

The HAADF image of Fig. 6a shows a precipitate, labeled A, at the end of an α_2 lath (2) that is partially disappearing in between precipitates A and B (see S8-Fig. 6), which are surrounded by γ lamellae except in the lateral interface, where an α_2 lamella, named (1), exists. The quantitative EDX map of the A precipitate shows a high Mo content (see S8-Fig. 6) with a composition of 48.9Ti–32.7Al–6.7Nb–1.7Si–10Mo (at%) together with the HRSTEM-HAADF image, Fig. 6b, and its FT confirm that it is the β_o phase. This A precipitate has three interfaces in the upper part, two with α_2 lamellae (1) and (2) and the third with the

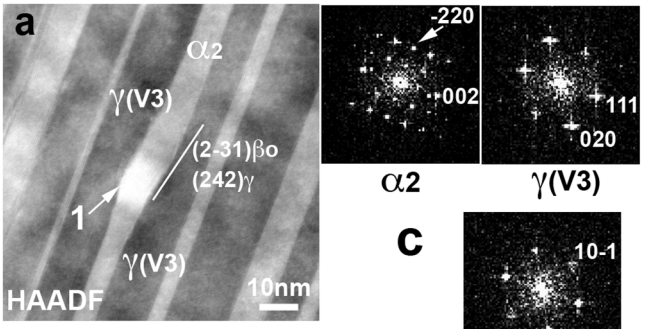

b

%at	Al	Si	Ti	Nb	Mo
γ	45.5	2.4	44.2	4.6	3.3
α_2	32.5	2.8	56.4	4.3	4.0
1-β_o	33	3.0	47.2	5.8	11

Fig. 5. TNM$^+$*I* sample; STEM at 300 kV. (a) HRSTEM-HAADF image; (b) Quantitative analysis from the EDX maps (I_{beam}=0.3 nA). Label (1) β_o precipitate; (c) FT of the HRSTEM image for α_2, γ(V3) and the precipitate β_o.

intermediate γ lamella. The HRSTEM-HAADF image, Fig. 6c, taken at the interface between the α_2 (1) and the γ lamellae, as well as its FT, evidence that this γ lath possesses the orientation termed variant V2. This A precipitate is also surrounded at the right and lower sides by another γ lamella, and the HRSTEM-HAADF image taken at its interface with the α_2 (2) lamella is presented in Fig. 6d, showing that this γ lath has another orientation (named as variant V1). The interfaces between γ lamellae (V1 and V2) with α_2 are flat showing the typical OR [42]:

$$(002)_{\alpha_2} \| \{111\}_{\gamma}$$

and

$$[\bar{1}\bar{1}0]_{\alpha_2} \| [\bar{1}10]_{\gamma_{V1}}$$

$$[\bar{1}\bar{1}0]_{\alpha_2} \| [01\bar{1}]_{\gamma_{V2}}$$

Moreover, the HRSTEM-HAADF image on this β_o precipitate and the γ phase, Fig. 6e, shows that the trace of the interface plane between β_o and γ_{V1}, indicated as a thin white line, maintains the directions $[111]_{\beta_o} \| [\bar{1}10]_{\gamma}$ along the interface, but changes its interface plane from $(1\bar{1}0)_{\beta_o} \| (111)_{\gamma}$ at the top of the image to $(2\bar{3}1)_{\beta_o} \| (224)_{\gamma}$ at the bottom of the image. Similar results were obtained for the precipitate B presented in the supplementary information, S8-Fig. 6. Finally, it should be noted that in another area just above the one shown in the images of Figs. 6a and S8-Fig. 6, which is presented in the supplementary information (S9-Fig. 6a), the α_2 lamella (1) is being divided in two parts by another γ lath growing in the middle. The HAADF image and the EDX map of Al show the co-existence between the dissolving α_2 lath, which is disappearing, and the γ lath growing at its expense. This is clearly evidenced by the EDX map and the analysis of S9-Fig 6a, showing that region 5 has a composition in between the ones of α_2 and γ phases.

3.3. Lamellar colonies after IF

In samples TNM$^+$*F* obtained after the series of internal friction measurements, the α_2 vol fraction measured in edge-on condition from HAADF and DF images is 25 %, so slightly smaller than in the initial samples TNM$^+$*I*, which is in agreement with measurements conducted before and after creep tests on the same alloys [19]. This is due to the dissolution of α_2 phase during high temperature exposure, giving place to a not homogeneous distribution of the α_2 phase as can be observed in the HAADF image of Fig. 7a where the α_2 lamellae appear in white contrast; compare area (1) with areas (2), (3) and (4) where α_2 laths

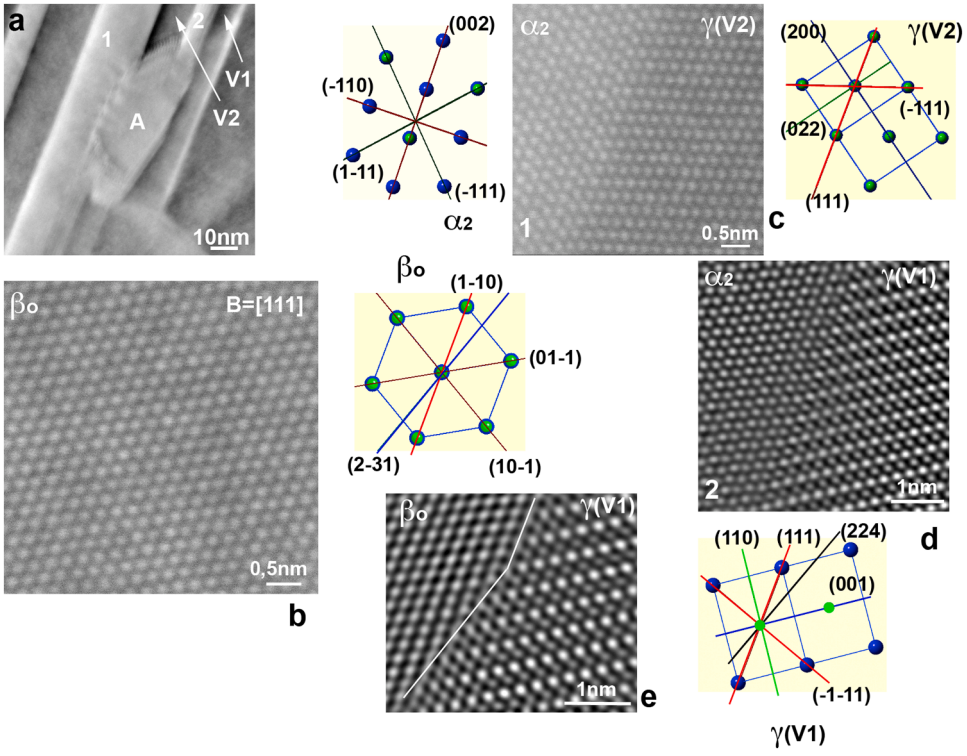

Fig. 6. TNM$^+$*I* sample; STEM at 300 kV. (a) STEM-HAADF image showing a precipitate labeled A as well as the α_2 lamellae labeled as 1, 2; (b) HRSTEM-HAADF image of the A precipitate; (c, d) HRSTEM-HAADF images at the interfaces between α_2 and γ(V1) and γ(V2) lamellae; (e) HRSTEM-HAADF images at the interface between β_0 and the γ(V1) variant. The oriented crystal lattices of the α_2 phase and the γ(V1) and γ(V2) variants are also represented: Al atoms are green and Ti atoms are blue.

were transformed into γ lath. The parallel micro diffraction pattern, taken in edge-on condition in the region of the Fig. 7a, shows that all six possible variants of γ lamellae are present, together with α_2 phase (see S10-Fig. 7a). In addition, in the areas 2 and 3 of Fig. 7a, the disappearance of some α_2 lamellae is observed. Here, the γ lamella at the right and left side of the α_2 phase corresponds to the same variant and there are no remaining traces of α_2 inside the new broader γ lath. On the contrary, when the disappearing α_2 lath is located in between two γ

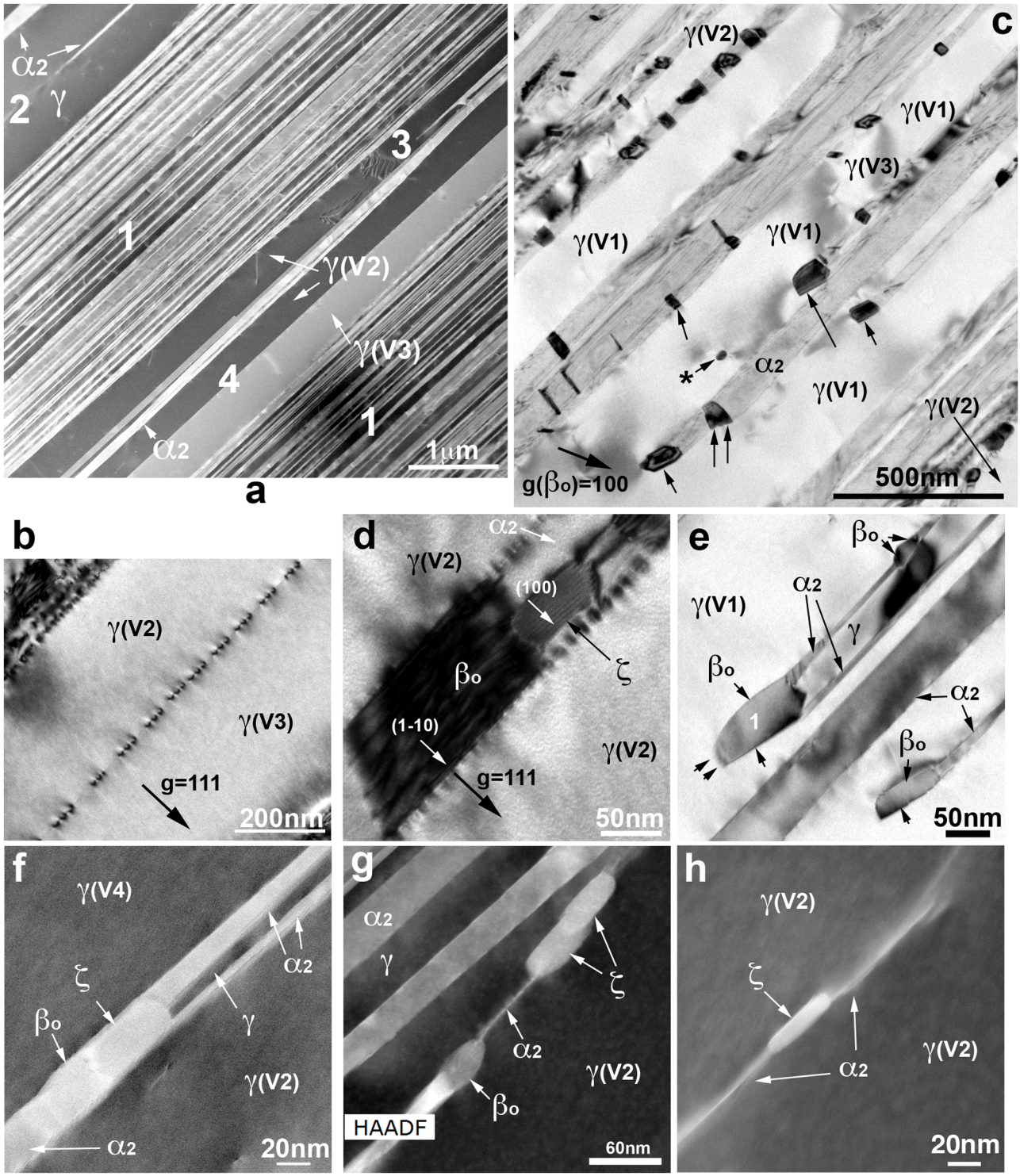

Fig. 7. TNM$^+$*F* sample; TEM/STEM at 200 kV in edge-on condition. (a) STEM-HAADF image showing regions 1 with high density of α_2 lamellae (white) and regions 2, 3 and 4 with γ lamellae wider than 300 nm; (b) BF image of the interface between variants γ(V2) and γ(V3) from the area 4 in the image (a); (c) BF image out of the edge-on condition in which the β_o and ζ precipitates appear black in diffraction condition; (d) BF image for α_2-γ(V2) of a small zone of the α_2 lamella indicated in the image (a). The diffraction vectors are g=1–10 of the β_o phase, g=100 of the ζ silicide and *g*=111 for γ(V2); (e) BF image for the α_2 and γ lamellae; the arrows indicate the interface plane γ−β_o deviating from the interface plane γ−α_2; (f) STEM-HAADF image for the α_2 and γ lamellae, showing β_o and ζ precipitates and a very thin γ lamella growing inside α_2 and stopped by ζ; (g) STEM-HAADF image for the α_2 and γ lamellae, showing a very thin α_2 lamella remaining in between two precipitates; (h) STEM-HAADF image for the α_2 and γ lamellae showing a very thin α_2 lamella remaining around a ζ precipitate.

lamellae in pseudo-twin orientation relationship, area 4, misfit dislocations remain at the γ/γ interface such as is observed in the BF image of Fig. 7b, which corresponds to the interface between the V2 and V3 variants. In the BF image of Fig. 7c, taken in diffraction condition for several β_o precipitates and silicides, a rather high density of precipitates can be observed and many of them are sharing an interface. In particular, the BF image of Fig. 7d was acquired at the α_2 lath between areas 3 and 4 in Fig. 7a, where two precipitates are observed inside the α_2 lath: a β_o precipitate with 8 at% of Mo spans over the full width of the lamella and the silicide (with a high content in Si, lower in Mo and higher in Nb), which is in contact with β_o on one side. The EDX maps and the electron nano diffraction patterns of these two precipitates are included in the supplementary information, S11-Fig. 7d. The diffraction patterns show that:

$$(1\bar{1}0)_{\beta_O} \| (300)_{\zeta} \| (111)_{\gamma} \| (002)_{\alpha_2}$$

and

$$[001]_{\beta_o} \| [011]_{\zeta}$$

with these directions close to the $[01\bar{1}]_{\gamma} \| [\bar{1}\bar{1}0]_{\alpha_2}$

Most of the precipitates in Fig. 7c are inside the α_2 lamellae whereas other (labeled with arrows) are located at the end of the α_2 lamellae that are disappearing. Some of such precipitates, as shown in Fig. 7e taken in BF and in edge-on condition for the interfaces α_2-γ, are of β_0 phase (10.5–14.0 at% Mo). Some of them, for instance the precipitate labeled (1), delay the progress of the γ lamella, whose growing inside the α_2 lath is causing its disappearance. In addition, the precipitates pointed with an arrow at the end of α_2 lamellae (Fig. 7c and e) have an interface with the γ phase always in the same orientation corresponding to the traces of the planes $(224)_{\gamma V1}$ and $(2\bar{3}1)_{\beta_o}$, as determined from the nano diffraction patterns of the precipitate β_o(1) and the variant γ_{V1}, which are shown in S12-Fig. 7e of the supplementary information. Finally, it should be noted that the interface labeled with two arrows in Fig. 7e has a comb-shape feature with its teeth (so the interfaces γ-β_0) parallel to the traces of the planes $(224)_{\gamma V1}$ and $(2\bar{3}1)_{\beta_o}$.

It must be remarked that, as a consequence of the disappearance of the α_2 lamellae, some small precipitates (labeled with an * in Fig. 7c) remain isolated inside the individual γ lamellae. The details of such precipitates are included in the supplementary information S13-Fig. 7c, where the EDX map allows identify them with silicides. The HAADF image, Fig. 7f, taken in edge-on condition for both the α_2 and γ lamellae, shows an α_2 lath in between two γ variants V2 and V4 in which one β_o precipitate (10.6 at% Mo) and one ζ silicide (24.1 at% Si and higher Nb content, i.e., 10.1 at%) are in contact. The details of EDX maps are presented in the supplementary information, S14-Fig. 7f. Additionally, at the right of the silicide, in Fig. 7f it is also observed that the central part of the α_2 lamella is transforming in a γ lamella, which propagates internally, whereas on the contrary, at the left of the precipitates, the local α_2 lath has not lost its integrity. Here, the ζ precipitate seems to partially block the disappearance of the α_2 lamellae, and this effect on retarding the disappearance of the α_2 lamellae is observed not only in Fig. 7e and f, but also in Fig. 7g where the broadening of the γ lamellae at the expenses of the α_2 is blocked, or retarded, by the presence of the β_o and ζ precipitates. In Fig. 7g, an extremely thin portion of α_2 phase, with a length of about 60 nm, is seen in between two silicides (with ζ≤60 nm) at the right and one β_o precipitate at its left. This means that when the segment of the α_2 lath will finally disappear, the silicides will become isolated inside the γ phase, in a similar way as the silicide labeled with * in Fig. 7c, in agreement with previous results [43]. The details of the EDX maps are given in the supplementary information S15-Fig. 7g. A similar result is observed in Fig. 7h, where another precipitate ζ (of 50 nm length and less than 20 nm thickness) retards the disintegration of the α_2 lamella in which it was previously formed. Finally it should be remarked that long portions of α_2 lamellae, with β_o and ζ precipitates at its tips and its interior, were observed fully isolated inside the γ phase. These results constitute a clear evidence of the influence of Si, through the presence of ζ precipitates, on the retention of the α_2 lamellae, in contrast with previous observations [44].

Fig. 8a, taken by STEM-HAADF in edge-on conditions for the interfaces γ/α_2, shows a series of α_2 lamellae with several precipitates (A1, A2, A3) at the ends in contact with the γ_{V4} lamella. Some precipitates (A4 and A5) are in contact with B1 and B2 precipitates, which remain at the interface with γ_{V4} lamella. Finally, three precipitates (A6, B3 and A7) are lined up at the extremity of a disappearing α_2 lamella. The EDX maps and the quantitative analysis show that the A precipitates have a high content of Mo whereas B precipitates are Si-rich (see S16-Fig. 8a in supplementary information). In Fig. 8b the nano diffraction patterns corresponding to the Fig. 8a allow identifying the variants γ_{V2} and γ_{V4} as well as the α_2 lamellae and the A precipitates, which are indexed as β_o phase. From these diffractions the following OR are deduced:

$$(1\bar{1}0)_{\beta_o} \| (002)_{\alpha_2} \| (111)_{\gamma} \quad \text{and}$$

$$[111]_{\beta_o} \| [\bar{1}\bar{1}0]_{\alpha_2} \| [01\bar{1}]_{\gamma_{V2}} \| [1\bar{1}0]_{\gamma_{V4}}$$

The γ_{V2} and γ_{V4} variants are order domain related and all A precipitates exhibit an interface with the γ_{V4} variant. In addition, from the image of Fig. 8a and the nano diffraction patterns of β_o and α_2, the trace of the interface plane β_o/α_2 is deduced to be:

$$(11\bar{2})_{\beta_o} \| (\bar{4}40)_{\alpha_2}$$

Fig. 8c shows a BF of the same area of the sample but tilted by 35° around the axis direction $[01\bar{1}]_{\beta_o}$ The nano diffraction patterns confirm that the B precipitates are ζ silicides. From the diffraction patterns of the A(β_o) and B(ζ) precipitates obtained for the same orientation of the BF image, the following OR are deduced:

$$(01\bar{1})_{\beta_o} \| (300)_{\zeta}$$

and

$$[011]_{\beta_o} \| [012]_{\zeta}$$

In addition, the plane $(100)_{\beta_o}$ is quasi-parallel to the $(1\bar{2}1)_{\zeta}$, with a misfit of 3.5 %.

Fig. 8d shows the same α_2 lath in contact with two precipitates previously shown in Fig. 7f. The left nano diffraction pattern corresponds to the ζ precipitate with a zone axis $[012]_{\zeta}$. Tilting back the sample −35° (same tilt as in Fig. 7f) but maintaining g(ζ)=300 and g(β_o)=01–1, the two diffraction patterns on the right, with zone axis $[111]_{\beta_o}$and $[001]_{\zeta}$ for the β_o and ζ precipitates, were obtained . From these diffraction patterns it is deduced that the six $\{300\}_{\zeta}$ equivalent planes are parallel to the six $\{110\}_{\beta_o}$ planes, verifying the following OR:

$$\{110\}_{\beta_o} \| \{300\}_{\zeta}$$

and

$$[111]_{\beta_o} \| [001]_{\zeta}$$

It should be remarked that the misfit between the planes $\{110\}_{\beta_o}$ and $\{300\}_{\zeta}$ is very small (−0.66 %). Besides, taking into account the diffraction pattern of the γ_{V2}, γ_{V4} and the α_2 lamellae, for such crystalline orientation it can be concluded that:

$$(1\bar{1}0)_{\beta_o} \| (0\bar{3}0)_{\zeta} \| (111)_{\gamma_{V2}} \| (111)_{\gamma_{V4}} \| (002)_{\alpha_2}$$

In the supplementary information S17-Fig. 7g, equivalent results are shown for the two silicides ζ and the precipitate β_o of Fig. 7g.

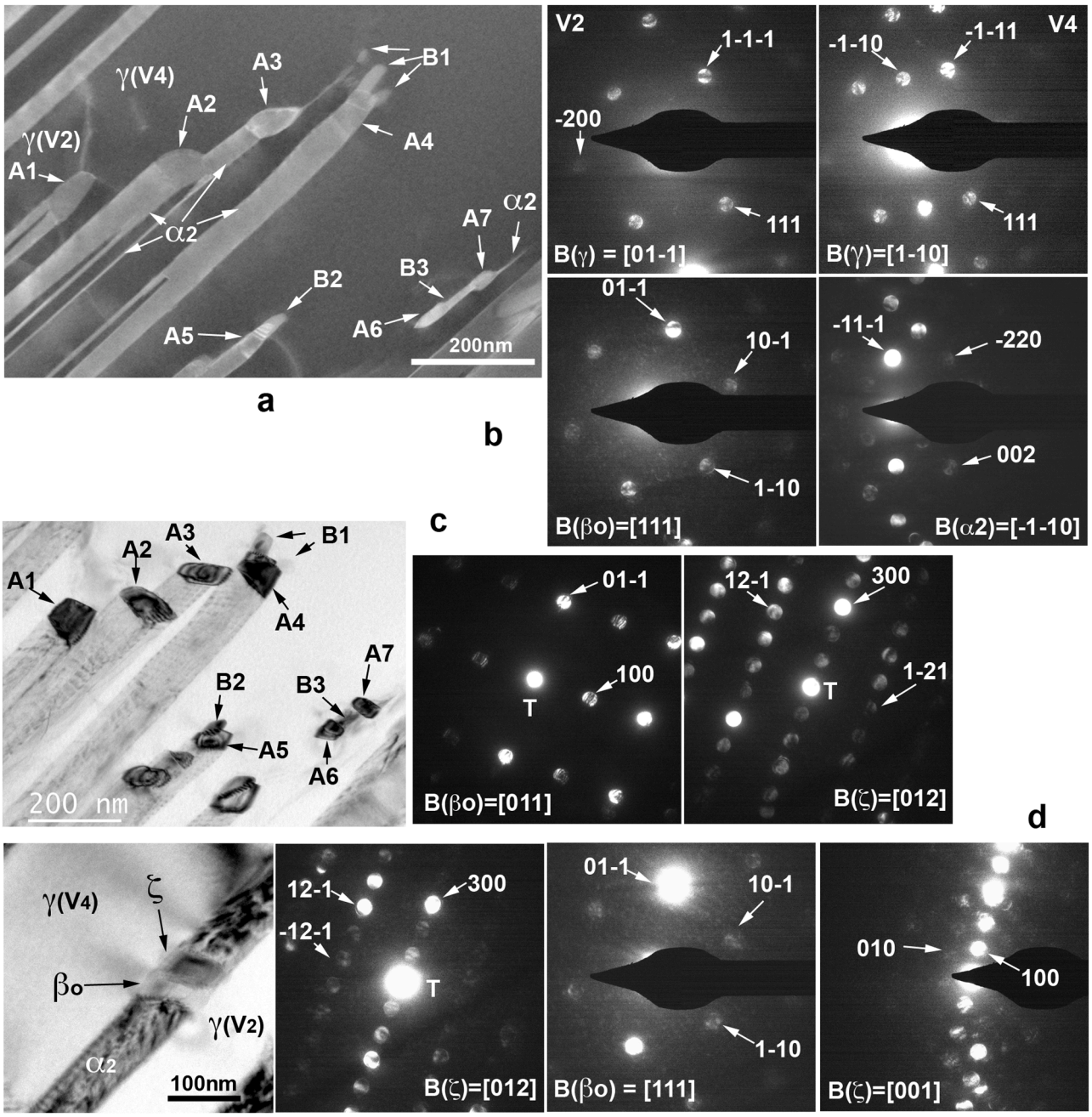

Fig. 8. TNM^{+}*F* sample; TEM/STEM at 200 kV. (a) STEM-HAADF image, showing β_o(Ai) and ζ(Bi) precipitates; (b) Near-parallel nano diffraction for the variants γ(V2) and γ(V4), α_2 lamellae and β_o precipitates under the same tilt conditions than in Fig. (a); (c) BF image and near-parallel nano diffraction patterns for β_o and ζ precipitates, in the same area after tilting 35° the sample around [01–1]β_o; (d) BF image and near-parallel nano diffraction patterns of the ζ precipitate (zone axis [012]ζ) shown in Fig. 7f, after tilting 35°. The near-parallel nano diffraction patterns of the precipitates β_o (zone axis [111]β_o) and ζ (zone axis [001]ζ) are also shown for the same sample orientation than in Fig. 7f.

4. Discussion

At present there is large accumulated information about the microstructure and the mechanical properties of γ-TiAl alloys published in the literature [3–8]. In particular a great effort is being devoted to understand and master the mechanisms associated to high temperature creep resistance, with regard to applications of γ-TiAl alloys in aeronautic engines. To open the discussion, let us remember three of the experimental evidences that were established in the scientific literature:

- The deformation at high temperature is controlled by the dislocation motion in the γ phase through a combined process of gliding plus climbing, being the second mechanism, controlled through vacancy diffusion.
- The inter-lamellar spacing of the α_2 and γ lamellae inside the lamellar colonies is a key factor to improve the creep resistance. This is basically associated with the fact that in thin lamellae the nucleation and motion of dislocations is prevented.
- At high temperature the employed γ-TiAl alloys undergo an evolution of the microstructure, associated with the equilibrium phase diagrams [6,45,46], in which the α_2 lamellae slowly disintegrate being transformed or incorporated to γ lamellae.

Then, at elevated temperatures, as it is the case of turbine blades, the

diffusion processes become thermally activated and α_2 transform to γ through interface diffusion, in order to accommodate the atomic element concentration of each phase. However, as the solubility of the α_2 and γ phase for each element is different, some precipitation should occurs, once again, controlled by interdiffusion processes. On one side interdiffusion through the α_2/γ interfaces will promote the broadening of the γ lamellae. As a consequence, sources of dislocations and its motion could be activated inside the γ phase and, subsequently, contribute to a loss of the creep resistance. On the other side, the nucleation and growth of precipitates by interdiffusion inside the α_2 phase could prevent the motion of the α_2/γ interfaces, thus sustainably delaying the loss of creep resistance. Thereby, the knowledge of the atomic diffusion processes and the associated evolution of the microstructure becomes the key factor to understand and improve the creep resistance of engineering γ-TiAl alloys.

The Ti and Al self-diffusion was studied in the binary Ti-Al system by several authors [21–25]. Diffusion of other alloying elements and their site occupancy were also discussed in several works [20,23,47], but the diffusion coefficients or their activation energies for diffusion were only rarely measured, e.g. Nb in α_2 phase [22] and Mo in β_o phase [28]. All these results are summarized in the supplementary Table ST-1. In addition, internal friction measurements [29,30] allow quantifying the influence of Nb and C on the Ti diffusion in α_2 phase, associated with the binding energy of these atoms with vacancies. This is an important point because Ti diffusion is a key factor in the interdiffusion processes involved in the transformation of α_2 lamellae into γ lamellae and the increase of the activation energy for Ti diffusion entails delaying such diffusion processes to higher temperature [31] and indirectly making the alloy more creep resistant.

4.1. Microstructure evolution and OR of the phases

The TNM$^+$ alloy contains 0.3 at% C, but in the present study no carbides were observed meaning that carbon remains in solid solution in the different phases α_2, γ and β_o, mainly in the α_2 phase as shown in S2-Fig. 1b, in agreement with previous works on the same alloy [19,29]. Indeed, the interstitial solubility of O and C in binary γ-TiAl alloys were studied by Menand et al. [47], which measured a C-solubility of 0.22 at % in γ-phase and 1.2 at% in α_2 phase at 1000 °C. These results were confirmed in Nb-containing alloys [48] and in TNM alloys derivates with several contents of C [32], which estimated a maximum C-solubility of 0.25 at% in γ-phase and about 1.5 at% in α_2 phase, with an overall C-solubility limit for the TNM alloy between 0.75 and 1.0 at%. The six-fold higher solubility in α_2 phase than in γ-phase is associated with the 6Ti-octaedral sites in α_2 phase as the preferential atomic environment of the interstitial C atoms [47]. As a consequence of the high C-solubility, the precipitation of carbides, particularly of H-type, is usually observed in γ-TiAl alloys with C content well above 0.5 at% [32,49]. Thus no carbides were expected in TNM$^+$ alloy, as confirmed in the present work.

Another interesting point concerns the ω_o phase. Although its precipitation inside β_o phase is currently observed in Nb-rich γ-TiAl and TNM alloys [50,51], the present work shows that it is absent in TNM$^+$ alloys. There is no simple explanation for this result, but could be related to the fact that Mo is a strong β-stabilizer [7] and when increasing the Mo content a stabilization of the β_o phase with respect to the ω_o phase occurs [52]. However, TNM and TNM$^+$ alloys have the same overall Mo content and the microanalysis carried out in this work shows that the content of Mo in β_o is only slightly higher in TNM$^+$ than in TNM alloys and not seems to justify the suppression of the ω_o phase. Moreover, the precipitation of ζ silicides with higher amount of Nb decreases the Nb concentration of the surrounding environment preventing the ω_o precipitation. In addition of this effect, we propose that the presence of C could be responsible for the inhibition of ω_o precipitation inside the β_o phase, through a simple mechanism in which the interstitial C atoms in β_o phase will prevent the collapse of the $\{111\}_{\beta_o}$ planes required for the nucleation of the ω_o phase, see the crystal lattices schema in a recent review [53]. It can be concluded that C in TNM$^+$ alloy is in solid solution, with the absence of carbides and ω_o precipitation. Indeed, the present study shows that the only precipitates present in TNM$^+$ alloy, which can influence the evolution of the nano-lamellar α_2/γ microstructure, are the β_o precipitates and the ζ silicides.

The present work shows that both precipitates β_o and ζ exhibit a high degree of coherence with the α_2 and γ lattices and the lattices orientation relationships were determined in TNM$^+$ alloy and presented in Figs. 3 to 8 in Section 3. The determined OR are compared with those from the literature and included in the supplementary Table ST-2, where an overview of the OR observed for all phases in γ-TiAl alloys is presented. However, among the diversity of OR, for the coexistence of two phases or, perhaps what is more important, for the nucleation and growing of one phase inside another, the more relevant OR are those with the smaller mismatch between both lattices. This mismatch can be evaluated through the misfit parameter for the interatomic distances, particularly for the denser atomic rows included in the OR, and also through the misfit of the interplanar distances of both lattices, particularly for those planes belonging to the observed OR. The misfit of all the relevant planes and directions in between the different phases were analyzed, and the interplanar distance misfits are presented in the supplementary Table ST-3, whereas the interatomic distance misfits are summarized in the supplementary Table ST-4.

4.2. Atomistic models in relationship with diffusion

The presented results show that the precipitates β_o and ζ nucleate and grow inside the α_2 phase during high-temperature aging. In this section an atomistic explanation is offered to understand how such processes could take place. A three-dimensional (3D) description of the three involved phases α_2, β_o and ζ is presented in the supplementary information S18-Fig. 9, just to remember the main similarly oriented axis directions and planes for each lattice, according to the OR experimentally observed in the present work and presented in Table ST-2. In the following, all the information from the TEM study, i.e. the OR and the mismatch between the different lattices, are used to simulate the relationship between each pair of phases. Then, the correlations found for the atomic rows and planes will be considered to describe the transition from one lattice to the other, and to give, a description of the plausible diffusion processes occurring during the nucleation and growth of the precipitates.

4.2.1. Model for the correlation of β_o with the α_2 phase

In this simulation, the lattices of the α_2 and β_o phases (S18-Fig. 9) are superimposed in a way that the most dense atomic rows of both phases are in coincidence. In the schematic drawing of Fig. 9a, both lattices are plotted with the $[111]_{\beta_o} \| [-1\,-1\,0]\alpha_2$ directions perpendicular to the paper. All atomic columns are dense rows and the interatomic distance is 0.2882 nm in α_2 and 0.2764 nm in β_o, with a misfit of −4.2 % (see Table ST-4). Atomic columns with the sequence Ti-Al in β_o are practically coincident with those of Ti-Ti and Ti-Al in the α_2 phase and some other are slightly rotated, see the atomic labels indicated in Fig. 9d. It is worthy to remark that the atomic planes misfit and the interatomic distance misfit of β_o-α_2 exhibits higher values than the misfit of β_o-ζ (see Tables ST-3 and ST-4), what means that the coherence of the β_o precipitates is smaller with the α_2 phase than with the ζ silicides.

Lets us now analyze the involved diffusion mechanisms. On one hand, *ab initio* studies [54,55] indicate that Si, Mo and Nb prefer to occupy the Al sublattice in the β_o phase. On the other hand, the experimental results of microanalysis, Figs. 1, 3 and 5, show an amount of Ti in β_o of about 50 at% and the other 50 at% is shared by Al, Si, Mo and Nb. Then, at the temperatures at which β_o precipitates are nucleated inside the α_2 phase, the Ti atoms must be locally expelled from the α_2 lattice, at least to transform the Ti-Ti columns of α_2 to the Ti-Al(Si, Mo, Nb) atomic columns of β_o. This process will be possible through the exchange of Nb

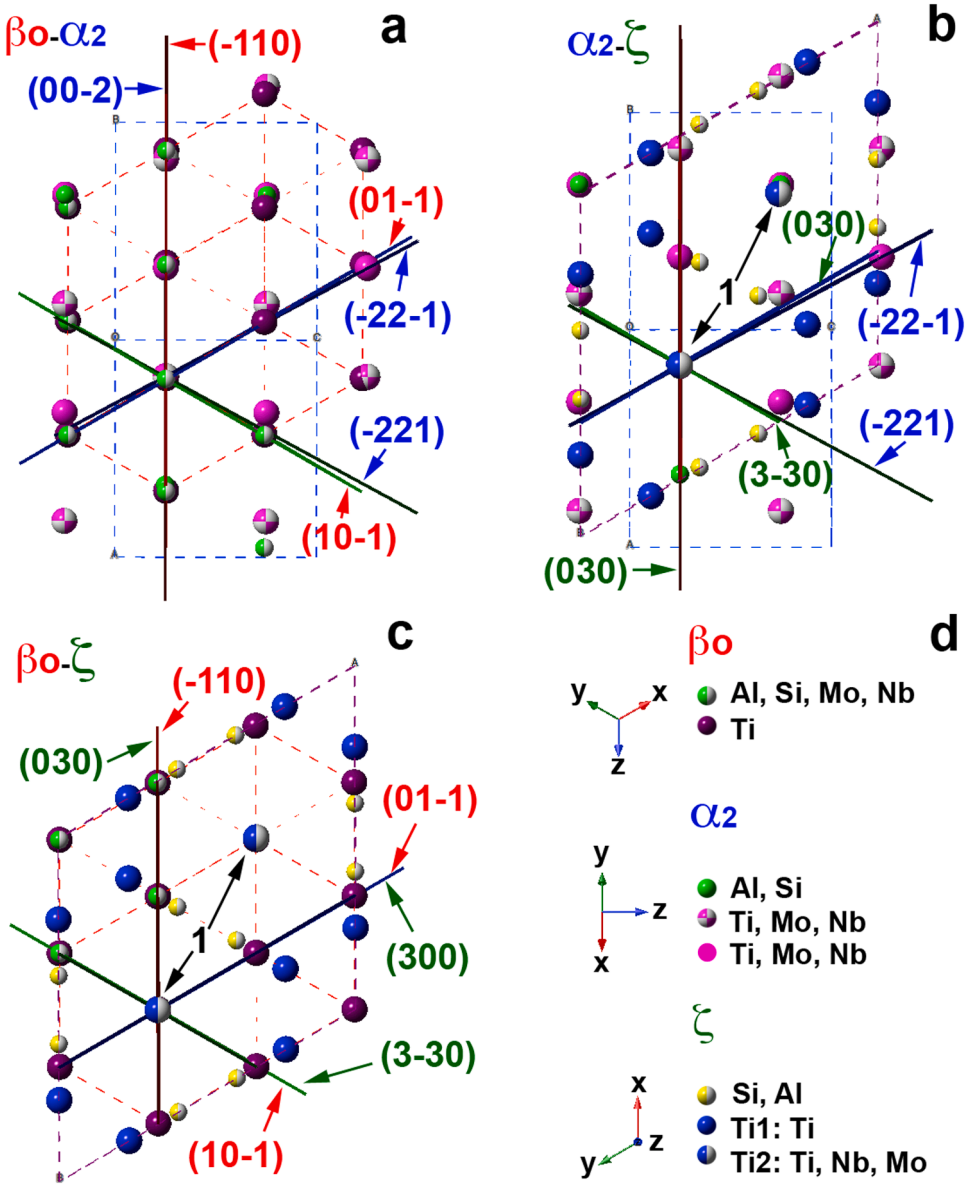

Fig. 9. Projection of the atomic lattices and crystallographic correlation for each pair of phases, where the main correlated planes are indicated in the same colors as the phase label. (a) Projection of the β_o and α_2 phases with the directions $[111]\beta_o$ || $[-1-10]\alpha_2$ normal to the paper; (b) projection of the α_2 and ζ phases with the directions $[-1-10]\alpha_2$ || $[001]\zeta$ normal to the paper; (c) projection of the β_o and ζ phases with the directions $[111]\beta_o$ || $[001]\zeta$ normal to the paper; (d) atomic symbols and color labels used for each phase, with the indication of the primary atom followed by the alternative atoms occupancy.

and Mo atoms that are at the Ti sites in α_2, which will diffuse out of the α_2 phase to enrich in Nb and Mo the Ti-Al atomic columns of the β_o precipitates. Particularly, the local amount of Mo must increase from about 2 at% in α_2 phase to about 10 at% in β_o. During this exchange, the dominant diffusion mechanisms will be the Ti diffusion in α_2, $E_{Ti}(\alpha_2)$= 3.2 eV [29], and the Mo diffusion in β_o phase, $E_{Mo}(\beta_o)$=3.55 eV [28]; these activation energies were measured by internal friction, see Table ST-1.

4.2.2. Model for the correlation of ζ with the α_2 phase

For the simulation of the relationship between the ζ silicides with the α_2 phase, both lattices, S18-Fig. 9, are superimposed in Fig. 9b, showing the coincidence of the dense atomic columns in the $[001]_\zeta$ || $[-1-10]_{\alpha 2}$ directions perpendicularly to the paper. The α_2 atomic columns and the ζ atomic columns, labeled as (1) in Fig. 9b, are dense atomic rows and the interatomic distances are 0.2715 nm for ζ and 0.2882 nm for α_2, respectively, with a misfit of 5.8 % (see Table ST-4). All other atomic rows belong to ζ and have a double interatomic distance of 0.5430 nm. In the silicide, both Si and Al share the same atomic sites and, because of symmetry order, it is expected that Ti atoms filled one atomic site labeled Ti-1, whereas the other atomic site Ti-2 should be shared by Ti, Nb and Mo, see the atomic labels of Fig. 9d. The atomic columns of ζ with a double interatomic distance are placed at one side and the other of the dense rows of the α_2 phase, one containing Ti and the other Si(Al). In this configuration, only a small shuffle displacement, on the right for one atom and on the left for the other, is required to make the transition from the ζ lattice to the α_2 lattice.

Regarding atomic diffusion, the measured atomic compositions of ζ and α_2 phases (see Figs. 1, 3, 5, S7 and S14) indicate that ζ contains double atomic amount of Nb (~8.5 to 10 at%) than the α_2 phase and, consequently, Nb must locally diffuse inside the α_2 phase to nucleate the silicides. The diffusion of Nb in α_2 takes place through the same vacancy mechanism than for Ti self-diffusion, but Nb is a slow diffuser with higher activation energy, $E_{Nb}(\alpha_2)$= 3.51 eV [22,25], as indicated in

Table ST-1. However, the main compositional difference is the high Si content of ζ (between 13 and 24 at%) in comparison with α_2 (less than 3 at%). This means that Si must be locally expelled by diffusion from the α_2 phase in order to nucleate the ζ silicides. Unfortunately, there are no data about Si diffusion in Ti_3Al or TiAl phases available in the open literature. Nevertheless, as Si and Ga occupy the Al sites in both lattices of Ti_3Al and TiAl, they could have similar diffusion behavior and Ga diffusion was studied by Herzig et al. [56]. Assuming this similarity, it could be expected that Si diffuses via anti-structural defects in the Ti sublattice, but perhaps with a much lower activation energy than the one for Al self-diffusion, as is the case for Ga atoms measured in TiAl, $E_{Ga}(\gamma)$= 3.04 eV [56], see Table ST-1 for comparison.

4.2.3. *Model for the correlation between β_o and ζ phases*

The presented experimental TEM results evidenced the simultaneous presence of β_o and ζ precipitates, see Figs. 3,4, 7 and 8, showing different interfaces, which OR were analyzed and summarized in Table ST-2. In Fig. 9c, see also the 3D plot in S18-Fig. 9, the superposition of the β_o and ζ lattices is shown, evidencing the coincidence of the $[111]_{\beta o}$ || $[001]_{\zeta}$ crystalline directions perpendicular to the paper. The atomic columns, denoted as (1) in Fig. 9c, correspond to dense rows with an interatomic distance of 0.2764 nm for β_o and 0.2715 nm for ζ, respectively, leading to a misfit of 1.8 %, see Table ST-4. The other atomic columns belonging to the ζ phase have a double interatomic distance of 0.5430 nm, being placed at one side and the other of the dense rows in β_o. The atomic labels in Fig. 9d show that one of these columns is of Ti atoms and the other of Si (Al) atoms and, once again, it is enough a small shuffle displacement of such atoms towards the right or towards the left to promote the transition from one lattice to the other. In addition, in Fig. 9c the coincident families of planes $\{110\}_{\beta o}$ || $\{300\}_{\zeta}$ are also plotted, according the OR experimentally observed in this work and shown in Table ST-2. They exhibit a very small misfit of −0.66 %, see Table ST-3, evidencing the high degree of coherence between both phases β_o and ζ. In the supplementary information S19-Fig. 9c, the simulated diffraction patterns of the superimposed β_o and ζ phases are presented, for different orientations, in order to illustrate the coherence between both phases. This high coherence will make easier the atomic inter diffusion between both phases. Silicon and Al atoms occupy the same atomic positions of Si in the Ti_5Si_3 lattice and, indeed, the experimental results of microanalysis (see Figs. 1,3 and S14) show that the Al+Si concentration is practically the nominal one of 37.5 at%. Nb and Mo occupy the Ti sites in the ζ lattice and the Ti+Nb+Mo concentration is again very close to the nominal one of 62.5 at%. This means that the diffusion processes will increase the concentration of Si and Nb in the ζ phase. In addition, the amount of Nb plus Mo is ranged between 12.5 and 14.4 at% and, consequently, Nb and Mo will occupy up to 23 % of the Ti sites. However, both phases β_o and ζ have a Ti content of about 50 at%, this means about 8 to 10 at% lower than the α_2 phase. The β_o phase accommodates a high content of Mo in the Al sites and the atomic columns coming from the Ti-Ti rows of the α_2 phase will be enriched of Mo atoms alternating with Ti. Similarly, the ζ phase has a high amount of Nb atoms, which will be enriching the Ti-Ti columns coming from the α_2 phase.

4.3. *Diffusion driven microstructure evolution*

In this section, all previous information will be used to describe the overall behavior of the nano-llamellar TNM^+ alloy at high temperature. The analysis will be focused on the diffusion driven microstructure evolution, aiming at the potential influence on the creep resistance.

The key point to increase the creep resistance is the γ/α_2 lamellar spacing, which, below a certain critical value, prevents nucleation and propagation of dislocations inside the γ phase lamellae [13–18]. Consequently, the strategy to enhance the creep resistance was to develop a microstructure fully composed of nano-lamellar γ/α_2 colonies [19], exhibiting very thin γ lamellae that are free of dislocations [19,29]. This goal would be reached and the problem definitely solved if this nano-lamellar microstructure would exhibit a long-term stability in the temperature range of potential service conditions, e.g. between 1073 and 1123 K (800 to 850 °C). Unfortunately, the equilibrium phase diagram as function of temperature promotes a slight evolution of the γ/α_2 fraction during high temperature exposure and a small decrease of the α_2 phase fraction, from 27 to 25 % as measured by TEM, in agreement with the observations made after creep tests [19]. This evolution proceeds by the dissolution and disintegration of the thin α_2 lamellae, which promote the thickening and coarsening of the adjacent γ lamellae, as observed in the present work, e.g. see Figs. 7,8 and S7, S8. This process is also favored by the interfacial energy decrease occurring when the α_2 lamellae disappear and the γ lamellae merge. However, this evolution must be driven by the diffusion processes required for the redistribution of the different atomic species through the local equilibrium phases. Indeed, the disappearance of the α_2 lamellae, as presented in Figs. 7,8, S7 and S8, requires the redistribution not only of the Ti and Al atoms through interdiffusion between α_2 and γ phases, but also that of the Mo and Si atoms because of the different solubility of these atoms in α_2 and γ phases, such as was determined by atom probe tomography, see Fig. 6 in Ref. [19]. The α_2 phase has higher solubility of Mo and Si than the γ phase and when the α_2 lamellae are disappearing the adjacent γ lamellae are not able to accommodate the excess of Mo and Si. The excess of Mo is eliminated through the precipitation of the β_o phase inside the α_2 lamella because the β_o phase is the only one which shows a high solubility for Mo, accommodating in some cases up to 13 at% Mo in its lattice, see Figs. 5b and S16-8a. As discussed previously, the dominant diffusion mechanisms during the nucleation of β_o will be Ti diffusion in α_2 and Mo diffusion in β_o. The activation energies of both mechanisms are presented in Table ST-1. These diffusion processes will be aided by the high coherence of the β_o and α_2 lattices in several planes and directions, see Fig. 9a and Tables ST-3 and ST-4. At the same time, the transformation of α_2 in γ will also generate a local excess of Si because of the large difference in solubility [19]. Nevertheless, the β_o precipitates formed inside the α_2 lamellae will dissolve a very small amount of the Si expelled from the α_2 lattice, which will be accommodated by the nucleation of the ζ silicides. A similar behavior of Si and Ga can be invoked again, with its activation energy intermediate between those of Ti in α_2 and Mo in β_o (see Table ST-1). Hence it is expected that the Si diffusion and the nucleation and growing of ζ silicides will occur simultaneously or just after the β_o precipitates. Consequently, both precipitates β_o and ζ will nucleate close to each other, such as was evidenced in Figs. 7d, 7f, 8a and S8. This is particularly favored by the high coherence of their atomic lattices, see Table ST-2, and promoted by the extremely low mismatch between both lattices, as shown in Tables ST-3 and ST-4. The high compatibility between both phases is also evidenced in Figs. 2 and 3, where silicides precipitate inside the β_o phase.

An important aspect of β_o and ζ precipitates is that they prevent or strongly retard the disappearance of the α_2 phase, as evidenced by the precipitates remaining at the boundaries of the α_2 lamellae being disintegrating, see Figs. 6a, 7,8 and S8. In Fig. 7(g, h) and Fig. 8a, the disappearing α_2 lamellae remain trapped at the β_o and ζ precipitates until the last moment of the final disintegration. This retardant effect of β_o and ζ precipitates is enhanced by an apparent slow dissolution kinetics of β_o and ζ in the γ phase because they remain isolated inside the γ lamellae, as shown in S8-Fig. 6a (precipitates C and D), Figs. 7 (g, h), S13-Fig. 7c and Fig. 8a (precipitates A6, A7, B3).

The dissolution of the β_o precipitates in the γ phase is delayed because of the high Mo content in β_o and the low solubility of Mo in γ. It has been observed, that a particular interface plane exists between both phases, well illustrated in Figs. 6a, 7 (c, e) and S8-Fig. 6, corresponding to the {2–31} planes of the β_o lattice, as determined by HRTEM (Fig. 6e). In Fig. 10a, a BF image of the precipitate 1 from Fig. 7e is presented to illustrate the β_o/γ interface and in Fig. 10(b, c) the lattice of both phases and the corresponding interface planes are indicated. It is worth to remark that the {2–31} planes of the β_o phase are planes with a high Mo

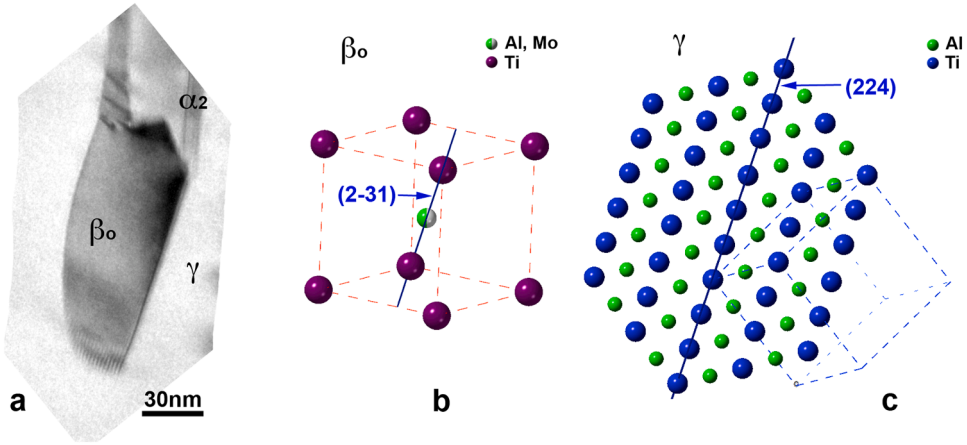

Fig. 10. (a) Bright field image of the same β_o precipitate, labeled (1) in Fig. 7e showing the flat interface with the γ lamella. Remark the comb-like BF contrast at the bottom of the precipitate; (b) lattice of the β_o phase in which the (2–31)β_o interface plane is indicated; (c) lattice of the γ phase showing the (224)γ plane parallel to the interface.

content and due to the low solubility of Mo in the γ phase, it seems that these planes block the diffusion from β_o to γ, preventing the dissolution of β_o parallel to those planes. This is observed at the bottom of the β_o precipitate in Fig. 10a, in which the interpenetration of the γ phase inside the β_o precipitate is evidenced by the comb-like contrast where the white teeth of γ phase penetrate inside the dark β_o phase.

The dissolution of ζ silicides once isolated inside the γ phase will be prevented due to its high Si content and the low Si solubility of the γ phase. In addition, atom probe tomography measurements [19] showed that ζ silicides dissolve a significant amount of interstitial C, see for instance C EDX map in S2-Fig. 1b, which could also delay the ζ dissolution, thus slowing down the disappearance rate of the α_2 lamella trapped at the ζ precipitates.

From the described scenario, it can be concluded that the β_o and ζ precipitates, which are nucleating and growing inside the α_2 lamellae during the exposure at high temperatures, have a retardant effect on the disappearance of the α_2 lamellae. Consequently, the thickening and coarsening of γ lamellae are also delayed and the final effect is a sustainable enhancement of the creep resistance.

5. Conclusions

The microstructure of a nano-lamellar TNM^+ alloy was characterized before and after a high-temperature exposure during internal friction measurements in order to study the occurring relaxation processes [29] in a temperature range from 600 to 1153 K. The highest temperature was chosen to be similar to the ones employed to test the creep resistance of this structural material [19]. The goal of the present study was to analyze the evolution of the microstructure in the nano-lamellar TNM^+ alloy at elevated temperatures in order to understand its thermal stability and the way in which such microstructure contributes to the enhancement of the creep resistance. At the light of the obtained results, the main conclusions are summarized as follows:

- Precipitation of carbides or ω_o phase was not observed and the reasons for this absence are discussed and justified.
- The orientation relationships (OR) of the dense planes and directions between the different phases α_2, β_o, ζ and γ were determined by micro and nano diffraction, HRTEM and HRSTEM. New original OR observations were found and compared with those from the literature. An overview is presented in the supplementary Table ST-2. In particular they are worthy of remark the two following OR:

$$\{110\}_{\beta_o} \parallel \{300\}_{\zeta} \quad \text{with} \quad [111]_{\beta_o} \parallel [001]_{\zeta}$$

and

$$(2\bar{3}1)_{\beta_o} \parallel (224)_{\gamma} \text{ with } [111]_{\beta_o} \parallel [\bar{1}10]_{\gamma}$$

- The misfit for the different planes and directions of the corresponding lattices were calculated in order to establish their coherence, which may promote the interdiffusion and the nucleation of the β_o and ζ precipitates inside the α_2 phase.
- The chemical concentration of the different elements in each phase was carefully measured by quantitative EDX maps in STEM mode, giving a clear idea of the required diffusion flow for each atomic species during the β_o and ζ precipitation processes. These exchanges were analyzed and discussed in terms of the coherence of their lattices.
- The dissolution and disintegration of the α_2 lamellae, along with the corresponding coarsening of the γ lamellae was studied simultaneously to the β_o and ζ precipitation, establishing the coupled behavior of such processes.
- The coupling between the β_o and ζ precipitation inside the α_2 phase and the final disintegration of α_2 lamellae in favor of the γ lamellae was analyzed and discussed in terms of the coherence of planes and directions of each lattice as well as the diffusion of the atomic species in each phase.

Finally it should be emphasized that the observed precipitation of β_o and ζ inside the α_2 lamellae prevents or retards the dissolution and final disintegration of the α_2 lamellae at high temperature. The reasons for this interaction have been discussed and give a clear explanation of the previously observed enhanced creep resistance in this nano-lamellar TNM^+ alloy. The acquired knowledge will allow further design concepts to improve the performances of intermetallic γ-TiAl based alloys.

Declaration of Competing Interest

The authors declare that they have no known competing financial interests or personal relationship that could have appeared to influence the work reported in this paper.

Acknowledgements

This work was supported by the Spanish MINECO through the project CONSOLIDER-INGENIO 2010 CSD2009–00013 and further Networks MAT2016–81720-Red Imagine and Red2018–102609T, as well as by the Consolidated Research Group, GIU-21/024, from the

University of the Basque Country (UPV/EHU). This work made use of the FEI-TITAN at the SGIKER facilities from the UPV/EHU.

Supplementary materials

Supplementary material associated with this article can be found, in the online version, at doi:10.1016/j.actamat.2023.119380.

References

[1] European Union Aviation Safety Agency (EASA), 2019 Aviation Environmental Report. https://www.easa.europa.eu/eaer/.
[2] Transport & Environment, 2018 Road Map to Decarbonising European Aviation. https://www.transportenvironment.org/discover/roadmap-decarbonising-european-aviation/.
[3] F. Appel, R. Wagner, Microstructure and deformation of two-phase γ-titanium aluminides, Mater. Sci. Eng. R 22 (1998) 187–268.
[4] H. Clemens, H. Kestler, Processing and applications of intermetallic γ-TiAl-based alloys, Adv. Eng. Mater. 2 (2000) 551–570.
[5] H. Kestler, H. Clemens, in: C. Leyens, M. Peters (Eds.), Titanium and Titanium Alloys, Wiley-VCH, Weinheim, Germany, 2003, pp. 351–392.
[6] F. Appel, J.D.H. Paul, M. Oehring, Gamma Titanium Aluminide Alloys, Wiley-VCH, Weinheim, Germany, 2011.
[7] H. Clemens, S. Mayer, Design, processing, microstructure, properties, and applications of advanced intermetallic TiAl alloys, Adv. Eng. Mater. 15 (4) (2013) 191–215.
[8] F. Apple, H. Clemens, F.D. Fischer, Modelling concepts for intermetallic titanium aluminides, Progr. Mater. Sci. 81 (2016) 55–124.
[9] H. Clemens, W. Wallgram, S. Kremmer, V. Güther, A. Otto, A. Bartels, Design of novel β-solidifying TiAl alloys with adjustable β/B2-phase fraction and excellent hot-workability, Adv. Eng. Mater. 10 (2008) 707–713.
[10] B.P. Bewlay, S. Nag, M.J. Weimer, TiAl alloys in commercial aircraft engines, Mater. High Temp. 33 (2016) 549–559.
[11] U. Habel, F. Heutling, C. Kunze, W. Smarsly, G. Das, H. Clemens, et al., Forged intermetallic γ-TiAl based alloy low pressure turbine blade in the geared turbofan, in: Proceedings of the 13th World Conference on Titanium, Hoboken, NJ, USA, John Wiley & Sons Inc, 2016, pp. 1223–1227.
[12] N.P. Lavery, D.J. Jarvis, D. Voss, Emission mitigation potential of ligtweight intermetallic TiAl components, Intermetallics 19 (2011) 787–792.
[13] K. Maruyama, R. Yamamoto, H. Nakakuki, N. Fujitsuna, Effects of lamellar spacing, volume fraction and grain size on creep strength of fully lamellar TiAl alloys, Mater. Sci. Eng. A 239-240 (1997) 419–428.
[14] T.A. Parthasarathy, M. Keller, M.G. Mendiratta, The effect of lamellar lath spacing on creep behavior of Ti-47at%Al, Scr. Mater. 38 (7) (1998) 1025–1031.
[15] A. Chatterjee, H. Mecking, E. Arzt, H. Clemens, Creep behavior of γ-TiAl sheet material with differently spaced fully lamellar microstructures, Mater. Sci. Eng. A 329-331 (2002) 840–846.
[16] G. DeWitt, J.S. Koehler, Interaction of dislocations with an applied stress in anisotropic crystals, Phys. Rev. 116 (1959) 1113–1120.
[17] J.P. Hirth, J. Lothe, Theory of Dislocations, John Wiley & Sons, New York, USA, 1982.
[18] F. Appel, U. Christoph, Coherency stresses and interface related deformation phenomena in two phase titanium aluminides, Intermetallics 7 (1999) 1173–1182.
[19] T. Klein, L. Usategui, B. Rashkova, M.L. Nó, J. San Juan, H. Clemens, S. Mayer, Mechanical behavior and related microstructural aspects of a nano-lamellar TiAl alloy at elevated temperatures, Acta Mater. 128 (2017) 440–450.
[20] D.G. Konitzer, I.P. Jones, H.L. Fraser, Site occupancy in solid-solutions of Nb in the intermetallic compounds TiAl and Ti_3Al, Scr. Metall. 20 (1986) 265–268.
[21] J. Rüsing, C. Herzig, Concentration and temperature dependence of titanium self-diffusion and interdiffusion in the intermetallic phase Ti_3Al, Intermetallics 4 (1996) 647–657.
[22] J. Breuer, T. Wilger, M. Friesel, C. Herzig, Interstitial and substitutional diffusion of metallic solutes in Ti_3Al, Intermetallics 7 (1999) 381–388.
[23] Y.L. Hao, D.S. Xu, Y.Y. Cui, R. Yang, D. Li, The site occupancies of alloying elements in TiAl and Ti_3Al alloys, Acta Mater. 47 (1999) 1129–1139.
[24] C. Herzig, T. Przeorski, Y. Mishin, Self-diffusion in γ-TiAl: an experimental study and atomistic calculations, Intermetallics 7 (1999) 389–404.
[25] Y. Mishin, C. Herzig, Diffusion in the Ti-Al system, Acta Mater. 48 (2000) 589–623.
[26] J. San Juan, P. Simas, T. Schmoelzer, H. Clemens, S. Mayer, M.L. Nó, Atomic relaxation processes in an intermetallic Ti-43Al-4Nb-1Mo-0.1B alloy studied by mechanical spectroscopy, Acta Mater. 65 (2014) 338–350.
[27] M. Castillo-Rodríguez, M.L. Nó, J.A. Jiménez, O.A. Ruano, J. San Juan, High temperature internal friction in a Ti-46Al-1Mo-0.2Si intermetallic, comparison with creep behaviour, Acta Mater. 103 (2016) 46–56.
[28] L. Usategui, M.L. Nó, S. Mayer, H. Clemens, J. San Juan, Internal friction and atomic relaxation processes in an intermetallic Mo-rich Ti-44Al-7Mo ($\gamma+\beta_0$) model alloy, Mater. Sci. Eng. A 700 (2017) 495–502.
[29] L. Usategui, T. Klein, M.L. Nó, S. Mayer, H. Clemens, J. San Juan, High-temperature phenomena in advanced intermetallic nano-lamellar γ-TiAl alloy. Part I: internal friction and atomic relaxation processes, Acta Mater. 200 (2020) 442–454.
[30] J. Ibáñez-Pérez, M.L. Nó, M. Oehring, H. Clemens, J.M. San Juan, Influence of Nb on Ti diffusion in γ-TiAl intermetallics studied by mechanical spectroscopy, J. Alloy. Compd. 867 (2021), 158880.
[31] J. San Juan, M. Oehring, H. Clemens, 2023 M.L. Nó. To be published.
[32] E. Schwaighofer, B. Rashkova, H. Clemens, A. Stark, S. Mayer, Effect of carbon addition on solidification behavior, phase evolution and creep properties of an intermetallic β-stabilized γ-TiAl alloy, Intermetallics 46 (2014) 173–184.
[33] T. Klein, M. Schachermayer, F. Mendez-Martin, T. Schöberl, B. Rashkova, H. Clemens, S. Mayer, Carbon distribution in multi-phase γ-TiAl based alloys and its influence on mechanical properties and phase transformation, Acta Mater. 94 (2015) 205–213.
[34] T. Klein, B. Rashkova, D. Holec, H. Clemens, S. Mayer, Silicon distribution and silicide precipitation during annealing in an advanced multi-phase γ-TiAl based alloy, Acta Mater. 110 (2016) 236–245.
[35] M. Kastenhuber, B. Rashkova, H. Clemens, S. Mayer, Enhancement of creep properties and microstructural stability of intermetallic β-solidifying γ-TiAl based alloys, Intermetallics 63 (2015) 19–26.
[36] R.C. Reed, The Superalloys. Fundamentals and Applications, Cambridge Univ. Press, Cambridge, UK, 2006.
[37] G.V. Somsonov, L.N. Olehremchuk, N.F. Podgrushko, I.A. Padchernyaeva, V. S. Fomenko, Relations between the electron work function and certain physical properties in silicides of group IV transition metals, Inorg. Mater. 12 (1976) 720–722. See also: Inorganic Solid Phases, P. Villars (Editor), https://materials.springer.com/isp/crystallographic/docs/sd_0378395.
[38] M. Es-Souni, R. Wagner, P.A. Beaven, Microstructure and phase relationships in a rapidly solidified dual phase alloy based on $Ti_3(Al,Si)+Ti_5(Si,Al)_3$, Mater. Sci. Eng. A 151 (1992) 69–75.
[39] S. Das, J.M. Howe, J.H. Perepezko, A high-resolution transmission electron microscopy studyof interfaces between the γ, B2 and α_2 phases in a Ti-Al alloy, Metall. Mater. Trans. A 27 (1996) 1623–1634.
[40] H. Inui, M.H. Oh, A. Nakamura, M. Yamaguchi, Ordered domains in TiAl coexisiting with Ti_3Al in the lamellar structure of Ti-rich TiAl compounds, Philos. Mag. A 66 (1992) 539–555.
[41] S. Zghal, S. Naka, A. Couret, A quantitative TEM analysis of the lamellar microstructure in TiAl based alloys, Acta Mater. 45 (1997) 3005–3015.
[42] M.J. Blackburn, The Science Technology and Applications of Titanium, Pregamon Press, Oxford, UK, 1970, p. p. 633. R.I. Jafee & N.E. Promisel.
[43] P.I. Gouma, M.J. Mills, Y.W. Kim, Characterization of the precipitation process in a TiAl-based alloy with carbon and silicon additions, Philos. Mag. Lett. 78 (1998) 59–66.
[44] S. Karthikeyan, G.B. Viswanathan, P.I. Gouma, V.K. Vasudevan, Y.W. Kim, M. J. Mills, Mechanisms and effects of microstructure on creep of TiAl-based alloys, Mater. Sci. Eng. A 329-331 (2002) 621–630.
[45] R. Kainuma, Y. Fujita, H. Mitsui, I. Ohnuma, K. Ishida, Phase equilibria among alpha (hcp), beta (bcc) and gamma ($L1_0$) phases in TiAl base ternary alloys, Intermetallics 8 (2000) 855–867.
[46] V.T. Witusiewicz, A.A. Bondar, U. Hecht, T.Y. Velikanova, The Al-B-Nb-Ti system. IV. Experimental study and thermodynamic re-evaluation of the binary Al-Nb and ternary Al-Nb-Ti systems, J. Alloys Compd. 472 (2009) 133–161.
[47] A. Menand, A. Huguet, A. Nérac-Partaix, Interstitial solubility in γ and α_2 phases of TiAl-based alloys, Acta Mater. 44 (1996) 4729–4737.
[48] C. Scheu, E. Stergar, M. Schober, L. Cha, H. Clemens, A. Bartels, F.P. Schimansky, A. Cerezo, High carbon solubility in a γ-TiAl-based Ti-45Al-5Nb-0.5C alloy and its effect on hardening, Acta Mater. 57 (2009) 1504–1511.
[49] H. Gabrish, A. Stark, F.P. Schimansky, L. Wang, N. Schell, U. Lorenz, F. Pyczak, Investigation of carbides in Ti-45Al-5Nb-xC alloys ($0\leq x\leq 1$) by transmission electron microscopy and high energy-XRD, Intermetallics 33 (2013) 44–53.
[50] M. Schloffer, B. Rashkova, T. Schöberl, E. Schwighofer, Z. Zhang, H. Clemens, S. Mayer, Evolution of the ω_o phase in β-stabilized multi-phase TiAl alloy and its effect on hardness, Acta Mater. 64 (2014) 241–252.
[51] L. Song, X.J. Xu, L. You, Y.F. Liang, Y.L. Wang, J.P. Lin, Ordered α_2 to ω_o phase transformations in high Nb containing TiAl alloy, Acta Mater. 91 (2015) 330–339.
[52] T. Klein, M. Schachermayer, D. Holec, B. Rashova, H. Clemens, S. Mayer, Impact of Mo on the ω_o phase in β-solidifying TiAl alloys: an experimental and computational approach, Intermetallics 85 (2017) 26–33.
[53] J. Ballor, T. Li, F. Prima, C.J. Boehlert, A. Devaraj, A review of the metastable omega phase in beta titanium alloys: the phase transformation mechanisms and its effect on mechanical properties, Int. Mater. Rev. 67 (2022), 2036401.
[54] D. Holec, R.K. Reddy, T. Klein, H. Clemens, Preferential site occupancy of alloying elements in TiAl-based phases, J. Appl. Phys. 119 (2016), 205104.
[55] N. Abddoshahi, M. Dehghani, L. Hatzenbichler, P. Spoerk-Erdely, A.V. Ruban, M. Musi, S. Mayer, J. Spitaler, D. Holec, Structural stability and mechanical properties of TiAl+Mo alloys: a comprehensive *ab initio* study, Acta Mater. 221 (2021), 117427.
[56] C. Herzig, M. Friesel, D. Derdau, S. Divinski, Tracer diffusion behavior of Ga as an Al-substituting element in Ti_3Al and TiAl intermetallic compounds, Intermetallics 7 (1999) 1141–1151.